INFN-LNL-288/2025

Sub-barrier fusion cross section measurements for $^{32}S + ^{96}Zr$

L. Barone[1,2], T. Berteotti[1,2], G. Montagnoli[1,2], A. M. Stefanini[2]

[1]Department of Physics and Astronomy "Galileo Galilei", University of Padua, Padua, Italy

[2]INFN, Laboratori Nazionali di Legnaro, Legnaro (Padua), Italy

Abstract

The fusion reaction near the barrier between the ^{32}S beam and the ^{96}Zr target was studied using the PISOLO electrostatic deflector [1]. In particular, by separating the evaporation residues (ER) from the sulphur beam, the $\sigma_f(E_b)$ excitation function was measured, i.e., the fusion cross section as a function of the incident beam energy. To obtain this result, it was first necessary to measure the angular distribution of the ER, obtained by normalising the fusion events to those of Rutherford scattering. The $\sigma_f(E_b)$ function thus obtained shows good agreement across the entire energy range considered with previous experimental results [2], whereas a discrepancy with calculations based on the Coupled Channels model (CC) emerges, especially at energies below the barrier. Overall, possible developments of the present work are: measurement of the excitation function over a larger set of energies below the barrier, and including neutron transfer channels in the coupling scheme.

1 Introduction

The heavy-ion fusion reaction is one of the main phenomena that have raised significant interest among nuclear physicists, especially concerning the unexpected behaviour at sub-barrier energies [3], [4]. The study of sub-barrier fusion is indeed rather useful to obtain insights into the reaction dynamics, which is strongly influenced by nuclear structure near the barrier.

The aim of the experiment thus consisted of direct measurements of fusion events, exploiting the Pisolo setup of the Laboratori Nazionali di Legnaro (LNL) to select and identify the ER of the fusion reaction between ^{32}S and ^{96}Zr. Once the data are gathered, the near-barrier fusion cross section is determined by relating the ER observed by PISOLO to Rutherford events observed by four Si-detectors included in the apparatus, thus avoiding dependence on the beam intensity, counting time, and thickness of the target. A final comparison with previous data and the CC model is then performed.

2 Theoretical framework

A first step concerned simulating the process and predicting the results by using the codes LISE++ [5] and CCFULL [6].

According to the semi-classical *Barrier Penetration model*, the fusion cross-section (σ_f) is determined by the energy E_{CM} with respect to the Coulomb barrier height (V_b) and the relative angular momentum l. Fusion occurs when the projectile has sufficient energy to overcome the barrier and the system has sufficient time to produce a compound nucleus (CN). The barrier radius between the two fusing nuclei is given by:

$$r_{max} \approx \rho_F (A_{^{32}S}^{1/3} + A_{^{96}Zr}^{1/3}) \simeq 11.2 \ fm \qquad (1)$$

where $\rho_F \approx 1.44 \ fm$ is the radius parameter. A classical estimate of the barrier in the CM frame is provided by the Coulomb potential evaluated at r_{max}:

$$V_c \approx \frac{1}{4\pi\epsilon_0} \frac{Z_{^{32}S} Z_{^{96}Zr} \, e^2}{r_{max}} \simeq 82.5 \ MeV \qquad (2)$$

which corresponds to $V_{c,LAB} \simeq 110.0 \ MeV$ in the LAB frame. Including quantum tunnelling effects (Hill-Wheeler [7]), the fusion cross-section is given (with some approximations) by the Wong formula [8], even though a significant disagreement is experimentally observed at sub-barrier energies. To explain this, it is necessary to include the internal degrees of freedom of the colliding nuclei, since the coupling between the various reaction channels strongly influences the cross section at energies below the Coulomb barrier, deviating from the 1-D description by Hill-Wheeler and Wong, which is suitable for structureless and spherical nuclei.

Analyzing fusion dynamics within the framework of the CC model, it is possible to account for the changes of the ion-ion potential due to the dynamic deformations and mutual orientation of the nuclear surfaces. Hence, the influence of the couplings on the dynamical Schrödinger equation causes a *barrier splitting* that affects the fusion probability, and the lowest barriers of this distribution lead to a significant enhancement of the fusion cross section. A further reaction channel that might contribute to the process is represented by nucleon transfer: if the Q-value of the reaction is positive, part of the surplus energy arising from that transfer can appear in the form of additional kinetic energy of the colliding fragments, thus helping them to overcome the barrier.

PACE4 [5] is a Monte-Carlo code we have employed to calculate the ER distribution following a fusion reaction. At the energy of $E_b = 120 \ MeV$, the resulting yields of residual nuclei are reported in Table 1.

Table 1: Most probable ERs after CN decay.

Residual	^{124}Cs	^{121}Xe	^{124}Ba	^{123}Cs	^{121}I
Frequency(%)	38.1	16.1	13.1	7.82	7.14

Focusing on ^{124}Cs (representative of the ERs produced), PACE4 provides the energy spectrum in terms of the number of events recorded per energy interval. Figure 1 displays the normalised counts along with the corresponding Gaussian fit, and in Table 2 μ and σ indicate the mean and standard deviation, respectively.

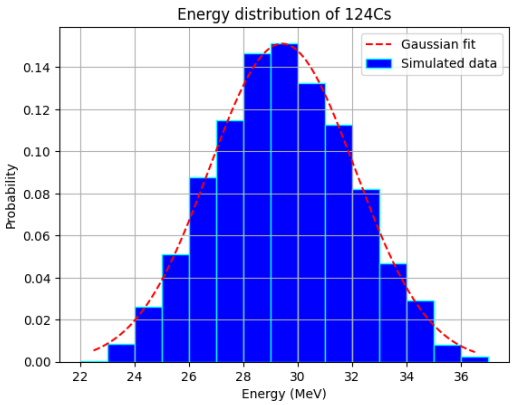

Figure 1: Energy distribution of simulated ^{124}Cs events.

Table 2: Gaussian fit parameters.

Observable	μ (MeV)	σ (MeV)
Energy (MeV)	29.42 ± 0.05	2.68 ± 0.05

ERs have energies much lower than E_b and, consequently, are easy to separate from the degraded ion beam. The CCFULL code [6] has been applied to include the internal degrees of freedom in the description fusion at sub-barrier energies. We have employed the Akyüz-Winther [9] potential with parameters are V_o=70.1 MeV, r_o=1.18 fm and a= 0.67 fm.

The coupled nuclear excitations have to be specified for both projectile and target, with the corresponding excitation energies, deformation parameter (β_λ) and multipolarities (λ). In this report, we show the results obtained, including only the vibrational states reported in Table 3.

Table 3: Coupled states for CCFULL calculations.

^{32}S states	^{96}Zr states
$2^+(2.230MeV)$; β_λ= 0.30	$2^+(1.750MeV)$; β_λ= 0.08
	$3^-(1.897MeV)$; β_λ= 0.28

A complete discussion about the quality of the results will be provided in section 5.

3 Experimental setup

Figure 2 is a scheme of the XTU-TANDEM accelerator. The sulphur particles are produced in the source (1) as negatively charged $q = -1e$ ions. After a preliminary acceleration stage of ~ 180 kV, the ions are injected into the Tandem accelerator, travelling (2) to the positive voltage terminal (4). During the experiment, this terminal was kept at a voltage of $\simeq 12$ MV or lower, by a laddertron charging belt (6). The entire accelerator tank (9) is filled with SF_6 at 7 atm in order to prevent dangerous electrical discharges along the accelerator itself. Inside the Faraday cage formed by the positive terminal itself, a carbon stripper (5) with a thickness of a few $\mu g/cm^2$ removes several electrons from the ^{32}S ions, with a distribution whose average value can be described by Sayer's semi-empirical formula [10].

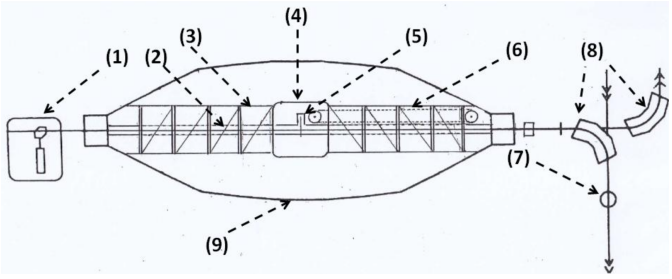

Figure 2: Tandem operating diagram (by F. Cervellera [11]). The following components can be identified: Platform housing the ion source (1); accelerating tube (2); column (3) supporting the high-voltage terminal (4), inside which the beam stripping station (5) is located; laddertron charging belt (6); beam diagnostics station (7); deflecting magnets (8); tank containing SF_6 gas at 7 atm (9).

The beam then continues its path, emerging from the cage and is strongly accelerated towards the exit. Outside the accelerator, thanks to a 90^o deflecting magnet (8), the final energy can be selected, and the beam is redirected to the experimental room where the PISOLO setup is located. Thanks to beam diagnostics (7) and secondary magnets, it was also possible to monitor and correct the characteristics of the ion beam in terms of aberration, collimation, and orientation.

It was chosen not to exceed 12 MV, collecting data only by decreasing the voltage value. This minimised problems of ferromagnetic hysteresis in the deflection magnet and electrical discharges in the electrostatic deflector of PISOLO. It was chosen to work exclusively with sulphur ions with charge state $+9e$. To this end, a dedicated LNL software [12] was used, which, by adjusting the TANDEM voltage and the NMR frequency associated with the deflecting magnet (8), allowed us to obtain the required beam energies. Then the fusion reaction of interest took place in the scattering chamber shown in Figure 3. The scattering chamber allows a rotation on the horizontal plane while maintaining the vacuum, an essential feature for measuring the fusion angular distribution.

At the centre of the chamber, maintained at a vacuum of approximately 10^{-6} $mbar$, a mobile target holder was placed, where a quartz and three layers of ZrO_2 (mass thickness 50 $\mu g/cm^2$) were mounted. While the former ensured the correct focusing of the beam during each run by means of the phenomenon of radioluminescence, the

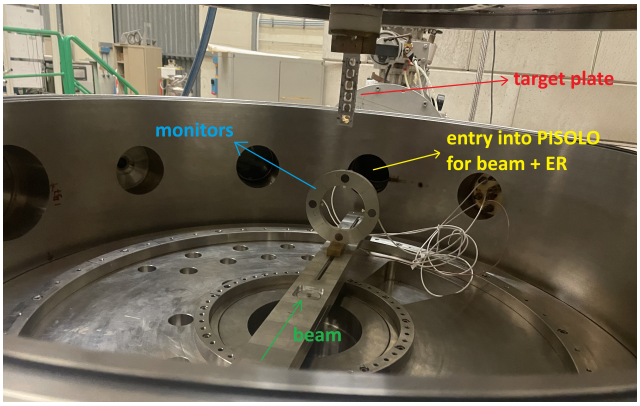

Figure 3: Interior of the scattering chamber, where the interaction between the beam and the target takes place and where the monitors are housed.

latter were the zirconium targets to perform the fusion reaction. The presence of oxygen, as well as of a ^{12}C support of 15 $\mu g/cm^2$ thickness, did not interfere with the measurements, given the large difference in mass and Z with respect to the Zr. In addition to the ERs, a large component of the beam is transmitted through the target, which constitutes the main experimental problem for the detection of the fusion products of interest. The beam and ERs therefore, enter the electrostatic deflector region where they are spatially separated due to their different electric rigidity.

As can be seen in Figure 3, four silicon detectors, each equipped with a collimator with a diameter 1.5 mm, were placed on a hollow circular support through which ER and the beam continue their path towards PISOLO. These "monitors", placed at an angle of $\alpha \simeq 16°$ with respect to the beam axis, were used to measure the Rutherford scattering, for normalisation purposes. Overall, the solid angle of the four monitors was $\Delta\Omega_{mon} = 0.167\ msr\ \pm 1\%$. Finally, with regard to the PISOLO telescope [1], a useful reference diagram is shown in Figure 4, where its structure is schematized and viewed from above.

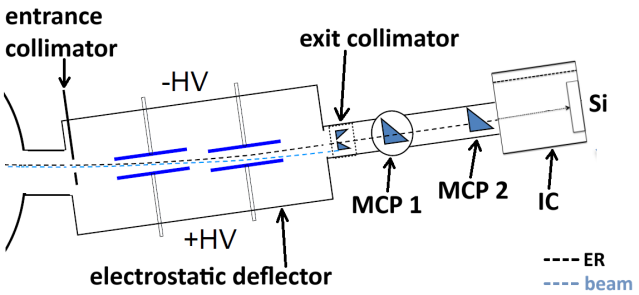

Figure 4: Images of PISOLO and its detectors seen from above. High Voltage (HV), Micro Channel Plates (MCP 1 and 2), Ionization Chamber (IC) and Silicon detector (Si).

As anticipated, the beam and ERs enter the deflector together, where a first collimator allows the definition of the angular range of the ions entering the electric field regions. These fields exploit the different electric rigidity of ER and ^{32}S, to separate their trajectories as much as possible. In particular, thanks to the geometry of the deflector and its electric fields, the following relationship between the ρ radii of curvature applies: $\frac{\rho_{ER}}{\rho_b} = \frac{m_b}{m_{ER}} \cdot \frac{q_b}{q_{ER}} \sim 0.13$. Therefore, since for the reaction under consideration both the mass and the charge of the ERs are much greater than those of the beam (b), a good separation is expected and, consequently, a high rejection factor of the beam ions entering the detector telescope is achieved. Indicatively, a reduction in the rate of detected sulphur ions around 10^7 is expected, thanks to the use of the electrostatic deflector.

The knowledge of the ERs, their average charge states, the required radius of curvature, and their energy allows for the evaluation of the proper fields using a C++ code developed at LNL. However, to check for the best conditions, it was necessary to correct the simulated voltages with the results of a series of measurements aimed at maximising the ERs transmission. The result was that, working with a sulphur beam at 120 MeV in the laboratory reference system, the optimum voltages had to be $|V_+| = |V_-| = 14.5\ kV$. After this selection, the ions pass through a second collimator at the deflector exit and enter the detector telescope composed by two Micro Channel Plates (MCP) for time-of-flight measurements (ToF), one ionisation chamber (IC) for ΔE measurements and a final silicon detector (with active area 600 mm^2) that provides both the residual energy of the ions E and their arrival time.

There are therefore in total five signals provided by PISOLO, three of which are ToF[1] and two are energy signals. So the detected ions can be identified and counted. The solid angle covered by PISOLO, i.e. the angle from which we observe the fusion process, is $\Delta\Omega_{fus} = 0.036\ msr\ \pm 1\%$. It is worth mentioning that approximately 30 data acquisition runs were conducted, each lasting between one and two hours, in the beam energy range $E_b \in [105, 120] MeV$ and in the angle range $\theta \in [-2, 7]°$ (in the horizontal plane and with respect to the beam direction). Figure 5 shows the overall electronic chain of PISOLO, where, in particular, an OR between signals from the monitors and from the silicon constitutes the trigger for the acquisition of the signals.

4 Data analysis

In order to determine the excitation function $\sigma_f(E_b)$, we have used the relation of the differential fusion cross section to the Rutherford one

$$\frac{d\sigma_f}{d\Omega}(E_b) = \frac{N_{ER}}{N_{mon}} \cdot \frac{\Delta\Omega_{mon}}{\Delta\Omega_{fus}} \cdot \frac{d\sigma_{Ruth}}{d\Omega}(E_b) \cdot \frac{1}{T \cdot t \cdot t_{IC}} \quad (3)$$

where $T = 0.45 \pm 4\%$ is the estimated transmission of the deflector, $t_{IC} = 0.81 \pm 1\%$ is the transparency of the grid separating the telescope high vacuum from the IC, and $t = 0.726 \pm 0.5\%$ is the cumulative transparency of the two MCPs. As can be seen, knowing the elastic scattering cross section as a function of beam energy, the only quantities to be determined are N_{ER} and N_{mon}, i.e. the total ER and Rutherford counts during a specific run.

[1] ToF1: MCP1-Si, ToF2: MCP1-MCP2, ToF3: MCP2-Si

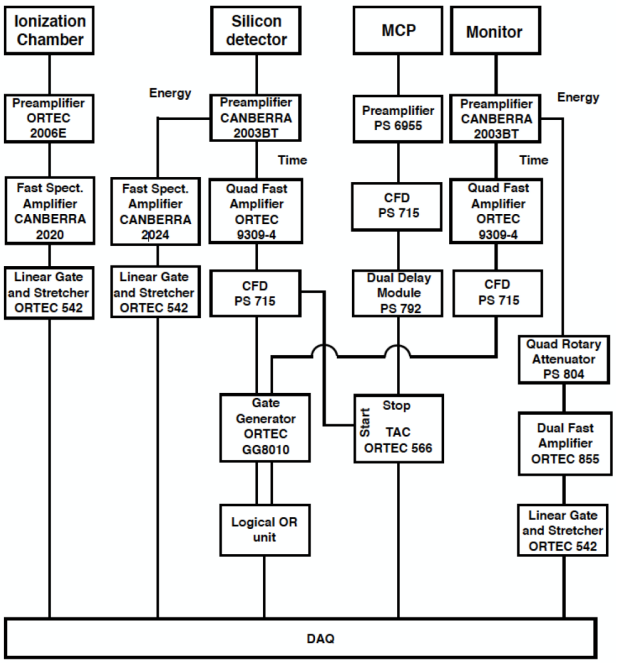

Figure 5: Scheme of the electronic chain of PISOLO.

The following paragraphs will explain the methodology for accurately obtaining these two quantities, which are indeed the core of our data analysis. The error associated to these counts has always been considered Poissonian, and wherever necessary, the uncertainties have been appropriately propagated (see equation 3). Then, once $\frac{d\sigma_f}{d\Omega}$ was obtained, a Gaussian function was used to fit the angular distribution of the fusion differential cross section at the laboratory energy $\tilde{E}_b = 105\ MeV$ (lower than the barrier). This is necessary to extract the total fusion cross section from the integral over θ, exploiting the independence of $\frac{d\sigma_f}{d\Omega}$ from the azimuthal angle. In fact, we can write

$$\sigma_f(\tilde{E}_b) = \int \frac{d\sigma_f}{d\Omega}(\tilde{E}_b)d\Omega = K_\theta \cdot \left.\frac{d\sigma_f}{d\Omega}\right|_\theta (\tilde{E}_b) \qquad (4)$$

This means that it is possible to relate the Gaussian differential cross section to the total cross section by means of a constant K_θ that depends on θ but is independent of the energy at which the angular distribution is measured, in the reasonable hypothesis that its shape does not vary in the measured energy range.

Consequently, to obtain σ_f at other energies, it will be sufficient to know only the value of the $\frac{d\sigma_f}{d\Omega}$ at the same specific angle. The choice of 105 MeV energy is purely arbitrary, as the angular distribution at any fixed energy is adequate. We chose to evaluate K_θ at $\theta = 2°$, which ensures good statistics.

4.1 The Rutherford cross section

The analytical form of Rutherford's differential cross section in the laboratory frame is

$$\frac{d\sigma_{Ruth}}{d\Omega}(E_b)[b/sr] = \left(\frac{Z_P Z_T e^2}{16\pi\epsilon_0 E_b}\right)^2 \cdot \cdot \left[\frac{1}{\sin^4(\alpha/2)} - 2\left(\frac{m_P}{m_T}\right)^2 + \left(\frac{m_P}{m_T}\right)^4\right] \qquad (5)$$

where Z and m are the atomic number and mass of projectile (P) and target (T), respectively, while E_b is the beam energy and α is the angle of the four monitors relative to the direction of the incoming sulphur ions, both in the laboratory frame.

It should be noted that a correction has been made to the beam energies used in the calculation of $\frac{d\sigma_{Ruth}}{d\Omega}$ (and consequently of $\frac{d\sigma_f}{d\Omega}$ and σ_f). In fact, it was assumed that the fusion reaction takes place at half the thickness of the target. This means that the effective energy to be considered for sulphur-zirconium interactions must be modified according to the Bethe-Bloch formula.
To obtain the number of Rutherford events in each run, the spectra of the four monitors were analyzed. An example can be seen in figure 6. N_{mon} is obtained by integrating the four spectra in appropriate channel windows and summing the results together.

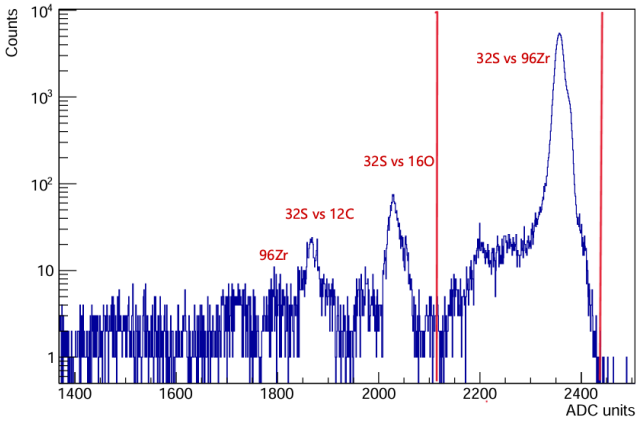

Figure 6: Example of a monitor energy spectrum. The peak of interest is the dominant one, and the integral is performed in the region delimited by the two vertical lines .

The integration has to be performed, for each run, on the same domain for all four monitors, to be appropriately defined from run to run. In fact, as can be seen in Fig. 6, in addition to the main peak, numerous secondary peaks can be clearly distinguished besides the main peak at lower energies, making it necessary to identify a criterion to establish how and what to integrate.

A rough analysis of the alternative possible interactions involving sulphur led to the conclusion that the main visible secondary peaks are due to the elastic interactions $^{32}S - ^{16}O$ and $^{32}S - ^{12}C$, and to recoiling ^{96}Zr ions. The large difference in energy of these different reaction products allowed us to clearly identify and distinguish the peaks. Thus an integration interval was always chosen that included only the main peak on the right. Table 4 shows the results of the runs at a fixed angle $\theta = 2°$, each with its own $\frac{d\sigma_{Ruth}}{d\Omega}$ and N_{mon} values. It also shows the average amount of energy E_{loss} of the sulphur ion in

half of the target, as well as the fusion counts N_{ER} (see Sect. 4.2).

4.2 The fusion differential cross section

To extract the N_{ER} values, we combined the measured quantities $(E, \Delta E, TOF1, TOF2, TOF3)$ associated with each ion detected by the telescope. It was chosen to construct energy-time matrices and, in particular, the 2D histograms considered were $E-TOF3$ and $\Delta E-TOF2$. Figure 7 shows an example of the plots that were constructed for each run, where the regions of integration with the corresponding counts obtained can be seen in red.

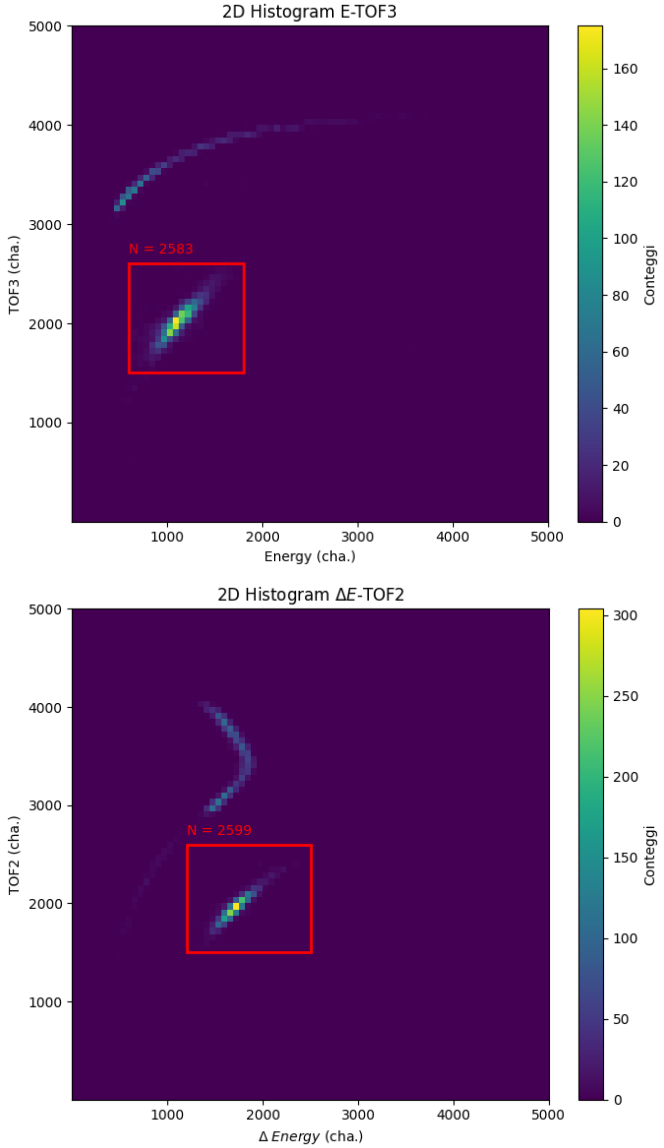

Figure 7: $E-TOF3$ and $\Delta E-TOF2$ matrices of the run 515. The red boxes indicate the chosen integration regions, and the values next to them are the number of ER counts.

Actually, combining energy and time allows ions to be distinguished based on their mass, since in the non-relativistic limit the $E \propto \frac{m}{ToF^2}$ relation applies. Moreover, the $E - TOF3$ and $\Delta E - TOF2$ pairs consist of signals that are independent of each other or combined in different ways.

The procedure for extracting N_{ER}, similar to that described in the 4.1 section, therefore consists of integrating a region of the two-dimensional histogram. The large difference in mass and energy between sulphur and ERs allowed for a clear-cut separation between the two contributions. In some cases, due to the presence of significant background, it was necessary to subtract the average counts obtained by integrating regions adjacent to those of interest. Once N_{ER} is obtained, the differential fusion cross section can be obtained using the (3) equation, leading to the total cross section.

4.3 Angular distribution analysis

As anticipated, once the differential fusion cross section at different angles was obtained, the next step was to construct the angular distribution of $\frac{d\sigma_f}{d\Omega}$ at the fixed energy $\tilde{E}_b = 105\ MeV$, varying the polar angle θ in the horizontal plane with respect to the beam direction between $-2°$ and $7°$. The obtained 1D Gaussian fit is shown in Figure 8, and the measured points are listed in Table 5.

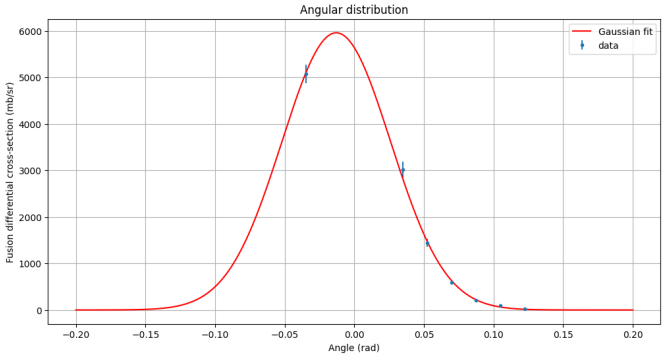

Figure 8: Gaussian fit of the angular distribution.

The functional form of the fit is a 1-D Gaussian with variable θ:

$$f(x) = Ae^{-\frac{(\theta-\theta_0)^2}{2s_\theta^2}}$$

where the fitting parameters are: $A = (6.0 \pm 0.2)\ b/sr$, $\theta_0 = (-0.013 \pm 0.002)\ rad$, $s_\theta = (0.039 \pm 0.001)\ rad$ and $\chi^2/d.o.f. \simeq 1.67$. By integrating this function on the solid angle, and exploiting the independence of the differential cross section from the azimuthal angle, equation (4) leads us to the value of the total cross section

$$\sigma_f(\tilde{E}_b) = (60 \pm 2)\ mb$$

The run 526 at $\theta = -4°$ was removed from the fit procedure, as it was affected by a large background, probably due to imperfect beam focusing.

Then it is possible to evaluate the K factor as follows:

$$K_{\theta=2°} = \frac{\sigma_f(\tilde{E}_b \simeq 105\ MeV)}{\frac{d\sigma_f}{d\Omega}\Big|_{\theta=2°}(\tilde{E}_b \simeq 105\ MeV)} = 0.020 \pm 0.001\ sr \tag{6}$$

and the conversion from differential to total cross section can be performed.

Table 4: Analysis performed for fixed-angle runs $\theta = 2°$. E_b is the energy of the sulphur beam in the laboratory, E_{loss} is the average energy loss in the target according to Bethe-Bloch, $E_{b,eff} = E_b - E_{loss}$ is the effective beam energy. $\frac{d\sigma_{Ruth}}{d\Omega}$ is the Rutherford differential cross section, and N_{mon} and N_{ER} are the counts of Rutherford scattering and fusion events, respectively.

run	E_b(MeV)	E_{loss}(MeV)	$E_{b,eff}$(MeV)	$\frac{d\sigma_{Ruth}}{d\Omega}$(b/sr)	N_{mon}	N_{ER}
515	120	0.20	119.8	97.42	$(252.3 \pm 0.5) \cdot 10^3$	2604 ± 51
516	117	0.20	116.8	102.49	$(365.6 \pm 0.6) \cdot 10^3$	3017 ± 55
517	114	0.21	113.8	107.97	$(402.5 \pm 0.6) \cdot 10^3$	2640 ± 51
518	111	0.21	110.8	113.90	$(473.2 \pm 0.7) \cdot 10^3$	2115 ± 46
519	108	0.21	107.8	120.33	$(459.3 \pm 0.7) \cdot 10^3$	1227 ± 35
520	105	0.21	104.8	127.32	$(397.7 \pm 0.6) \cdot 10^3$	515 ± 23

Table 5: Summary of the angular distribution data at $E_{b,\text{eff}} = 104.79\ MeV$: θ is scattering angle in the laboratory frame, N_{mon} and N_{ER} are the monitor and ER counts respectively and $\frac{d\sigma_f}{d\Omega}$ is the fusion differential cross section.

run	$E_{b,\text{eff}}$(MeV)	$\theta(°)$	N_{mon}	N_{ER}	$\frac{d\sigma_f}{d\Omega}$(b/sr)
521	104.8	2	$(119 \pm 0.3) \cdot 10^3$	160 ± 9	3.02 ± 0.18
522	104.8	4	$(305 \pm 0.6) \cdot 10^3$	81 ± 6	0.59 ± 0.05
523	104.8	6	$(725 \pm 0.8) \cdot 10^3$	30 ± 4	0.09 ± 0.01
524	104.8	3	$(249 \pm 0.5) \cdot 10^3$	161 ± 9	1.45 ± 0.08
525	104.8	-2	$(183 \pm 0.4) \cdot 10^3$	415 ± 14	5.07 ± 0.20
527	104.8	7	$(127 \pm 0.4) \cdot 10^3$	1.0 ± 0.7	0.02 ± 0.01
528	104.8	5	$(704 \pm 0.8) \cdot 10^3$	64 ± 6	0.20 ± 0.02

5 Results

The fusion cross sections at different beam energies has been obtained by applying (6) to the $515 - 520$ runs (Table 6).

The obtained excitation function is plotted in Figure 9

Table 6: Fusion cross-sections at different LAB energies.

run	$E_{b,eff}(MeV)$	$\frac{d\sigma_f}{d\Omega}\Big\vert_{\theta=2°}(b/sr)$	$\sigma_f(mb)$
515	119.8	17.69 ± 0.53	354 ± 18
516	116.8	14.90 ± 0.41	298 ± 15
517	113.8	12.48 ± 0.33	249 ± 12
518	110.8	8.97 ± 0.24	179 ± 9
519	107.8	5.66 ± 0.16	113 ± 6
520	104.8	3.02 ± 0.18	60 ± 2

together with the previous results [2] and the CCFULL calculations. The coupled channels are the 2^+ of ^{32}S and both 2^+ and 3^- states of ^{96}Zr, as indicated in the figure (the octuple vibration is very strong in ^{96}Zr).

The present experimental data well agree with those of Ref. [2], taking also in account that only the statistical uncertainties have been plotted for the present data, while a systematic error of 7-8% can be estimated for them, deriving from the uncertainties on the angles and energies of the beam,on the target isotopic corrections, and on the angular distribution fit. The CCFULL calculations are able to reproduce the data above and near the barrier, but fail at lower energies, probably due to the fact that nucleon transfer channels have not been included in the coupling scheme.

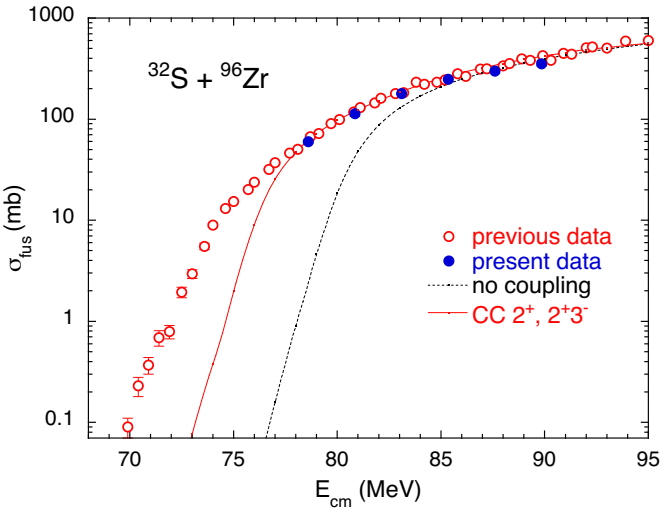

Figure 9: Fusion excitation function ^{32}S$-^{96}$Zr: in red the 6 data points reported in Table 6; in blue the results of Ref. [2] plotted with the reported 15% systematic error. The red and black lines are the results of the CCFULL calculations.

6 Conclusion

The experimental study of ^{32}S and ^{96}Zr fusion was successfully completed, using the PISOLO set-up of the LNL. The fusion cross-sections have been measured for several points near and above the barrier, and show a good agreement with previously published data for the same system. The CCFULL code, based on the CC model, gives results in good agreement with the present findings, in the measured energy range. At lower energies, we have indication, also from a comparison with previous results, that nucleon transfer channels should be explicitly considered in the CC calculations. Therefore, possible future devel-

opments based on this work may focus on extending the measured range to lower beam energies, together with a more detailed theoretical analysis within the CC model.

Acknowledgements

We are grateful to INFN-LNL for allowing us to carry out this experiment, in the frame of the "Advanced Laboratory" course for the master degree in physics at the Department of Physics and Astronomy of the University of Padova. Thanks are also due to Tommaso Dalla Valentina, who participated in the first part of the course. We also acknowledge the very professional work of the Tandem staff at LNL, which has made it possible to perform the present measurements.

References

[1] INFN Laboratori Nazionali di Legnaro. Pisolo telescope. https://www.lnl.infn.it/fisica-nucleare-csn3.

[2] H. Q. Zhang, C. J. Lin, F. Yang, H. M. Jia, X. X. Xu, Z. D. Wu, F. Jia, S. T. Zhang, Z. H. Liu, A. Richard, and C. Beck. Near-barrier fusion of ^{32}S+^{90,96}Zr: The effect of multi-neutron transfers in sub-barrier fusion reactions. *Physical Review C*, 82:054609, 2010. https://doi.org/10.1103/PhysRevC.82.054609.

[3] G. Montagnoli and A. M. Stefanini. *Nuclear Physics Notes*. 2024. To be published.

[4] V. Zagrebaev. *Heavy Ion Reactions at Low Energies*. Springer, 2019. https://doi.org/10.1007/978-3-030-27217-3.

[5] O. B. Tarasov and D. Bazin. LISE++: Exotic beam production with fragment separators and more. *Nuclear Instruments and Methods in Physics Research Section B: Beam Interactions with Materials and Atoms*, 266:4657–4664, 2008. https://doi.org/10.1016/j.nimb.2008.05.110.

[6] K. Hagino, N. Rowley, and A. T. Kruppa. A program for coupled-channel calculations with all order couplings for heavy-ion fusion reactions. *Computer Physics Communications*, 123:143–152, 1999. https://doi.org/10.1016/S0010-4655(99)00243-X.

[7] D. L. Hill and J. A. Wheeler. Nuclear constitution and the interpretation of fission phenomena. *Phys. Rev.*, 89:1102, 1953. https://doi.org/10.1103/PhysRev.89.1102.

[8] C. Y. Wong. Interaction barrier in charged-particle nuclear reactions. *Phys. Rev. Lett.*, 31:766, 1973. https://doi.org/10.1103/PhysRevLett.31.766.

[9] Ö.Akyüz and Å.Winther. Nuclear structure and heavy-ion physics. *Proc. Int. School of Physics "Enrico Fermi", Course LXXVII, Varenna, edited by R.A.Broglia and R.A.Ricci (North Holland, Amsterdam, 1981)*.

[10] R. O. Sayer. Semi-empirical formulas for heavy-ion stripping data. *Revue de Physique Appliquée*, 12(10):1543–1546, 1977. https://doi.org/10.1051/rphysap:0197700120100154300.

[11] INFN Laboratori Nazionali di Legnaro. Tandem accelerator. https://www.lnl.infn.it/tandem/.

[12] INFN Laboratori Nazionali di Legnaro. Beam energy and nmr frequency. https://userswww.pd.infn.it/~montag/GASP/Beam/Beam.html.